A Benchmarking Platform and a Control Allocation Method for Improving the Efficiency of Coaxial Rotor Systems

Joao Buzzatto , *Graduate Student Member, IEEE*, and Minas Liarokapis , *Senior Member, IEEE*

Abstract—**Coaxial rotors used on multirotor Micro Aerial Vehicles (MAVs) are complex aerodynamic systems that are typically treated in a simplified manner, operating in sub-optimal conditions. In this letter, we propose: i) an open-source benchmarking platform for coaxial rotor systems that allows us to analyse and improve their efficiency and ii) a map of the whole actuation domain of coaxial systems based on extensive experimentation. In particular, we test three systems built using off-the-shelf components and different rotor configurations. Results demonstrate the existence of a maximum efficiency boundary, which covers the whole thrust range of each system. We also analyze how this boundary changes with respect to the rotor configuration. We compare it with the performance of coaxial rotors controlled with the current standard method (i.e., equal commands for both rotors). Finally, we propose a control allocation strategy that improves the efficiency of coaxial rotors by up to 11 % over the current industry standard. Implementation on an octocopter with four sets of coaxial rotors validates the proposed methods across two different rotor separation designs and two different payload scenarios.**

Index Terms—**Aerial systems: mechanics and control, performance evaluation and benchmarking, aerial systems: applications.**

I. Introduction

SMALL scale, electric Unmanned Aerial Vehicles (UAVs) have been extremely popular in robotics over the last two decades [1], [2]. During this time, UAV concepts have grown in variety and complexity, both in terms of design and automation, but also aerodynamically. Aerodynamics research, however, is not the focus of the robotics community. So complex aerodynamic systems are usually treated in a simplified manner, often operating in sub-optimal conditions, and not enough research effort is put towards improving them. This is particularly evident in multirotor vehicles with coaxial rotors, where each motor/propeller pair is still treated as a single rotor [3]. Such rotor configurations are generally used in applications requiring high thrust but small vehicle footprint, such as in aerial manipulation [4], drone delivery [5], and to enable the development of new
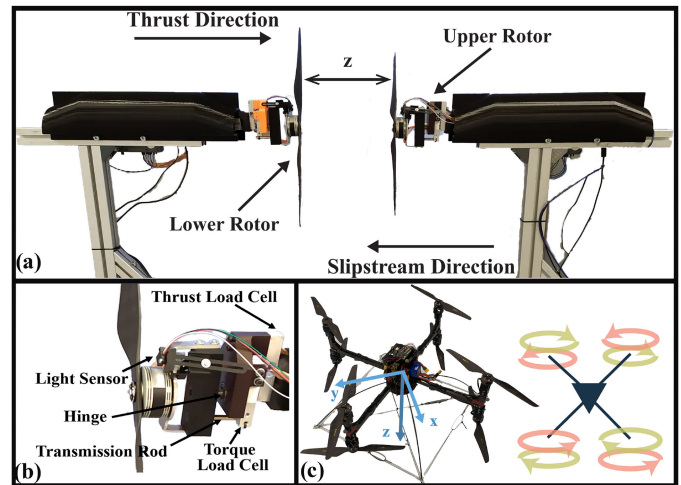
Fig. 1. Subfigure (a) presents the benchmarking platform designed to test coaxial rotors systems used on multirotor UAVs. Each side of the testing rig is equipped with force and torque sensors. Individual motor speed, applied voltage, and consumed electric current are measured. Everything is integrated and controlled by a LabView interface. Subfigure (b) presents a close-up view of the structure and the sensors of one unit of the benchmarking platform, where two load cells are used for measuring thrust and torque, and a light sensor measures the motor rotation speed. Subfigure (c) presents the rotor's spin direction and vehicle's reference frame.

vehicle concepts [6], [7]. Due to their heavy load capacity and rotor redundancy, coaxial multirotor systems are also employed in manned multirotor and transport applications [8]–[10], or even for space exploration [11]. However, despite the extensive range of applications and the potential of coaxial rotor systems, their behavior and characteristics are not fully understood. Most of the existing works investigate rotor separation and how it influences thrust and efficiency [12]–[16]. However, none of these works performs a throughout investigation in terms of speed range, focusing either on a specific operating condition (e.g., balanced torque) or on equal speeds and commands, with some exceptions. The authors in [17] performed extensive experiments to improve control, ignoring efficiency. Meanwhile, [18] presents a comprehensive study aimed at the acoustics of contra-rotating coaxial systems.

In this paper, we present: i) an open-source benchmarking platform for coaxial rotors that facilitates analysis and modelling, ii) experiments that demonstrate that there is an efficiency ceiling for each rotor pair and that such maximum efficiencies are larger than the efficiencies achieved by the standard control

allocation for coaxial rotors, also investigating how this efficiency ceiling changes with rotor separation, iii) a control allocation method that reproduces the efficiency ceiling in a single coaxial rotor set in static testing, and iv) a method to implement this control allocation on a multirotor vehicle. More specifically, we focus on counter-rotating coaxial rotors with fixed pitch propellers and equal upper and lower rotors built using off-the-shelf components. These considerations are necessary to exclude coaxial rotors of helicopters that have both rotors operating at the same speed and which are controlled with a swash-plates mechanism. Also, we consider only counter-rotating coaxial rotors because they are known for being about 5% more efficient than co-rotating coaxial rotors, according to [19]. Results demonstrate that the proposed method can improve efficiency up to 11% over the current industry standards. The results of this paper can be used to aid in the development of more efficient multirotor coaxial vehicles. Specifically, the methods presented here can help designers achieve the maximum possible efficiency of coaxial multirotors made with off-the-shelf components.

In this work, we purposefully avoid using some aerodynamics notions such as coefficient of power, thrust, torque, and Figure of Merit [19]–[21], as such non-dimensional quantities make the design process of aerial vehicles less straightforward when using off-the-shelf components. Another reason for not employing such metrics is that the literature still seems to lack proper definitions in the case of coaxial rotors. For coaxial rotors, most metrics involve some type of special operating conditions, such as equal thrust sharing between the rotors [22], equal rotational speeds [19], [21], [22], and net-zero torque [19], [21] that are used for traditional helicopters, which have different controls and operating conditions.

II. Benchmarking Platform for Coaxial Rotors

The benchmarking platform for coaxial rotors is made out of modular aluminum extrusions, and it comprises two identical units placed one in front of the other (see Fig. 1 (a) and (b)). Such units are aligned with the help of another long extrusion that holds the whole structure together. The design assumes that the propellers are mounted to generate forces only in one direction (i. e., pushing from left to right on Fig. 1), where the structure is reinforced with $45°$ bars. The rotors are aligned horizontally to provide more clearance for the air to flow around the room and dissipate. At the top-most part of each stand unit, the final extrusion holds all the sensors and electronics, allowing for easy and fast reconfiguration. To change the distance between the rotors, the two screws from each side should be relaxed to slide the extrusions to another position. Additionally, a black 3D printed case was placed over each stand unit to protect and cover the sensitive electronics and wires. The coaxial system's quantities of interest for this work are the induced thrust, torque, motor speed, applied voltage, and electric current consumed by each rotor. By measuring such quantities, it is possible to obtain the total induced thrust, torque, electrical and mechanical power, and efficiency of the whole coaxial system for any configuration tested. Every sensor on the platform is integrated into a LabView interface. The computer running the LabView program communicates with a National Instruments MyRIO development device that collects data from all sensors and sends commands to control the motors. The force and torque measurements are taken using appropriate load cells. The signal

from the load cells is first amplified and converted to digital using HX711 breakout boards. The MyRIO unit then collects the digital signal. Rotational speed from the motors is measured by employing a long-distance reflective switch (OPB732WZ from TT Electronics) and reflective tapes placed on the motors. FPGA and real-time software embedded on the MyRIO ensure that each pulse from the reflective switch is read, resulting in accurate speed measurements. Current is measured with an SEN-16408 KR Sense Current Sensor, placed in series with the Electronic Speed Controller (ESC) and the power supply. To measure voltage, we employed a voltage divider connected directly to one of the AD ports on the MyRIO. Finally, PWM signals from the MyRIO are sent to the ESC for motor control. Only two load cells are used to measure thrust and torque from the motor. At one end, the thrust and torque load cells are mounted on the same part. The other end of the thrust load cell is mounted on the platform's structure, while the other end of the torque load cell is free. Torque is measured by sensing the force a transmission rod exerts on the load cell. Such rod is attached to a part that is free to rotate with respect to the part where both load cells are mounted, and only the contact of the rod with the torque load cell provides resistance. However, to prevent the rod part and the rotor mounted on it from rotating in the other direction, the rod is fixed in contact with the load cell. Finally, an aluminum plate provides support where the motor is mounted. The plate is attached to the part containing the rod. Using 5 kg rated load cells with RMS error 0.05%, each stand unit is estimated to measure thrusts of up to 5 kg with precision of 2.5 g, and torques of up to 1.4715 Nm with a precision of 0.00073575 Nm. All the designs and code of the benchmarking platform, as well as supplementary materials, can be found at: http://www.newdexterity.org/coaxialbenchmarkingplatform

III. Experiments and Analysis

A. Experimental Procedure

All experiments presented here were performed in a large room to allow air circulation and avoid interference. Additionally, all coaxial experiments were performed on the same day, with only a couple of hours difference between the first and last test. The controlled temperature of the room (it was set to $21°C$) and the short interval between the tests performed with the same rotor also favored consistency, avoiding significant air temperature and humidity changes that could interfere with results. Each data point considered in this study followed the same measurement protocol through pre-programmed tests. The throttle command was ramped continuously from the previous set point to the next within 1 s. Then, the command was held constant for 3 seconds to allow adequate time for stabilization. Measurements were taken only at the end of the 3 seconds with constant command. Each point was the average of 20 samples collected from the sensors. The sampling frequency for all sensors was set to 50 Hz. Measurements were saved during run-time on a. csv file. All data was then imported and processed/analysed on MATLAB.

B. Single Rotor Experiments

Three sets of rotors are used. The main difference between the rotors is their KV, and the recommended propeller size. Table I summarizes the components comprising the rotors sets and the

TABLE I
COMPONENTS USED ON THE THREE ROTORS SET TESTED

Set ID	Propeller	Motor
1	T-Motor 22x6.6" NS Carbon Fiber	T-Motor MN501-S KV240
2	T-Motor 16.2x5.3" FA Carbon Fiber	T-Motor MN4014 KV400
3	APC 11x4.5" MR Plastic	Propdrive V2 35-36 KV910

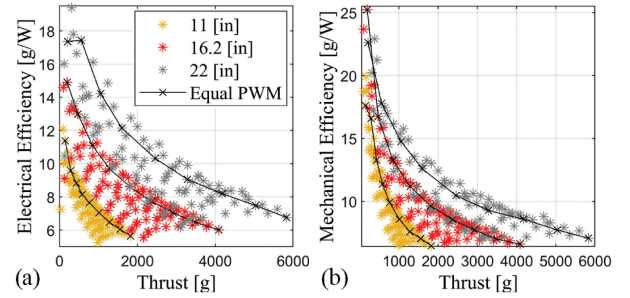| Set ID	ESC	Voltage [V]
1	T-Motor FLAME 100A 6-14S	25
2	T-Motor FLAME 100A 6-14S	22.2
3	T-Motor AIR 40A 2-6S	11.1

Fig. 2. Plots of mechanical and electrical efficiencies against thrust for all coaxial rotor sets tested at $z/D = 0.7$. Efficiency measurements plotted against thrust for the whole actuation domain create areas with clear efficiency ceiling $\mathbf{C}_\eta$. The results indicate that there is a corresponding maximum efficiency operating point for every desired thrust. Highlighted in black are the points of equal commands that for most of the thrust range, are not part of $\mathbf{C}_\eta$.

testing conditions. The simple single rotor experiments serve as a reference for the results obtained for the more complex coaxial rotor systems. The isolated sets of rotors were tested on the "Upper Rotor" position of the platform, while the "Lower Rotor" position was pushed far away and had nothing mounted on it. Additionally, the "Upper Rotor" position was kept at least half of the propeller's diameter away from the vertical extrusion to avoid any interference that could compromise the results. The testing itself consisted of a command swap from 40% to 95% of throttle divided into 20 equally spaced points. The testing results are presented on a dedicated website, the URL found in Section II. The main quantities of interest for this work are: thrust T, torque τ, mechanical η_m and electrical η_e efficiencies and rotor speed ω. The equations we used for calculating the efficiencies for the coaxial rotor system are:

$$\eta_m = \frac{T}{\tau_u\,\omega_u + \tau_l\,\omega_l}, \qquad (1)$$

$$\eta_e = \frac{T}{I_u\,V_u + I_l\,V_l}, \qquad (2)$$

where I is electric current, V is voltage and $*_u$ and $*_l$ indicate the quantities related to the upper and lower rotor, respectively. In both equations, the efficiency considered is the ratio between the total thrust divided by the system's total power, mechanical or electrical. The same principle is used for single rotor experiments, where just one term is used in the denominators. The second preliminary test evaluates if the structure holding the lower rotor can influence the readings of that rotor, as it is downstream to its induced flow. The same test described as the first preliminary test above is repeated for the lower rotor to check this interference. The "Lower Rotor" is positioned as far away as possible from the "Upper Rotor" in these experiments. Even though the upper rotor does not run during these tests, placing them far away simulates experiments performed for coaxial systems. The results from this second experiment are again presented on the website, as mentioned earlier. No significant differences are noticeable for the rotors with propellers of 22 and 16.2 inches in diameter, with a RMS difference of 2.71% for the 22 inches and 1.68% for the 16.2 inches. This indicates that the interference on the measurements by the structure downstream to the slipstream of the lower rotor is minimal and can be assumed to be negligible. For the rotor with a diameter of 11 inches, however, the difference in readings is significant, with a RMS difference of 8.91%. Based on these and other results, the minimum propeller size recommended for testing on this platform is 15 inches. Despite the significant interference of the structure on the readings for the 11 inches lower rotor, observations from coaxial experiments on such rotor pair can

still provide insightful information, and therefore the results are presented.

C. Coaxial System Experiments

The coaxial system experiments consist of swiping each motor's commands from 7% to 95%, divided into 10 equally spaced points, resulting in a total of 100 data points per test. With such tests, we obtain a map for the coaxial system that practically covers the whole actuation space of the rotor pair.

We investigate how the map characteristics (especially efficiency) change when varying the separation distance between the rotors. Since the tests consider three different rotor sizes, the spacing between the rotors is specified as the non-dimensional ratio z/D, where z is the distance between the propellers and D is the propeller diameter. The same set of ratios is tested for the three rotor sets. The values range from 0.1 to 1 divided into 7 equally spaced points, with z/D taking the following values: 0.1, 0.25, 0.4, 0.55, 0.7, 0.85, and 1. The range selected is typical for most multirotor vehicles having coaxial rotors as propulsion units and being constructed of common, off-the-shelf components.

For each rotor set, testing across all separation ratios results is 700 data points in total, where each data point has individual rotor information about the command sent, thrust, torque, voltage, current, and rotation speed. Presenting all the data in this paper is impossible. Thus we focus on displaying plots that combine multiple sets of tests. Whenever this was not possible or would result in a cluttered graph, we presented data for only one set of tests as an example. Fig. 2 shows mapping results plotting mechanical and electrical efficiency against thrust. Each rotor set displays an area with a clear upper boundary covering the whole thrust range. This indicates that every thrust along this range has a correspondent operating point on such a maximum efficiency boundary. Let us denote this condition for maximum achievable efficiency boundary, or efficiency ceiling, as $\mathbf{C}_\eta^*$. The super-script * can be ^{e} for electrical efficiency, ^{m} for mechanical efficiency or omitted to refer to both. Moreover, when highlighting the points corresponding to equal commands sent to both rotors (i.e., the current state-of-the-art control allocation), the curve it forms is below the curve formed by the upper boundary. This is observed for most of the system's thrust range and for both mechanical and electrical efficiencies. Furthermore, the same is true not only for the results shown in Fig. 2 but for all of
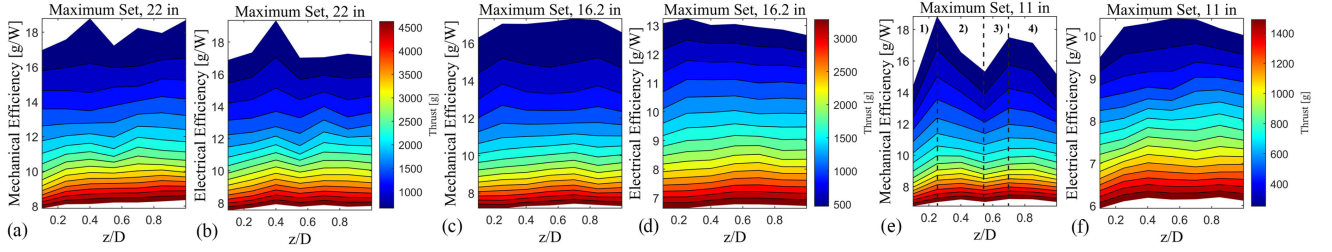
Fig. 3. $\mathbf{C}_\eta^m$ and $\mathbf{C}_\eta^e$ variation across rotor distances. The first two plots shows the results for the rotors with 22 inches propellers. The 16.2 inches rotors results are displayed in the third and fourth plots, while the results for the 11 inches rotors are in the last two plots.
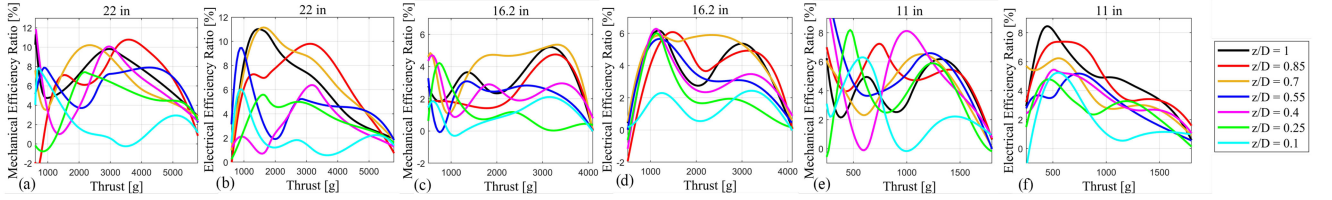

Fig. 4. Electrical and mechanical $\%\Delta\eta$ for all tests. The map results show the potential of efficiency gain for every thrust setting point and each rotor separation. (a) and (b) shows the results for the 22 inches rotors, (c) and (d) for 16.2 inches rotors, and (e) and (f) shows for the 11 inches rotors.

the experiments considered in this work. Therefore, we conclude with the following main observations: i) for a coaxial system with equal, counter-rotating electric rotors with propellers of fixed pitch, powered with the same source, there is a boundary of maximum efficiency, or efficiency ceiling $\mathbf{C}_\eta$, that covers the whole thrust range and ii) the condition of equal commands for both rotors is below the maximum efficiency boundary for most of the system thrust range. Fig. 3 displays how $\mathbf{C}_\eta$ changes with respect to rotor separation distances. The three sets of rotors produced different behaviors. Most notable, the 11 inches rotor displays considerable change, especially for $\mathbf{C}_\eta^m$. As shown in Fig. 3 (e), the change is characterized by four distinct regions: i) a region of lower $\mathbf{C}_\eta$ at the smaller separation of $z/D = 0.1$, where the efficiency increases with the separation, reaching a local maximum in between $0.25 < z/D < 0.4$, ii) $\mathbf{C}_\eta$ decreases with larger separations, going from a local maximum to a local minimal that occurs at about $z/D = 0.55$, iii) $\mathbf{C}_\eta$ starts to increase again with rotor separation, reaching another local maximum at around $0.7 < z/D < 0.85$, and finally iv) $\mathbf{C}_\eta$ decreases with increasing rotor separation, until the last separation ratio tested of $z/D = 1$. Despite still being present, the effect is much less pronounced for the $\mathbf{C}_\eta^e$ results, in Fig. 3 (j). Nonetheless, the behavior described seems to be magnified for larger $\mathbf{C}_\eta$, both electrical and mechanical. The 22 inches rotor set displays similar characteristics to the 11 inches set, albeit with less pronounced efficiency variations. For the 22 inches rotors, besides the relatively smaller efficiency variations compared to the 11 inches results, the two local maximums also seem to be closer together and absent for some thrust levels. This is also the case for most of the 16.2 inches rotors test results.

The following result attempts to quantify the difference between the efficiencies achieved by the equal commands case and $\mathbf{C}_\eta$. Since data points were collected based on motor commands and not on thrust setpoints, there is no point-to-point correspondence between thrusts measured for equal commands and thrusts measured at the maximum efficiency boundary. We used spline

curve fitting [23], obtaining a continuous proxy curve for both cases. This allowed a comparison using

$$\%\Delta\eta^* = \left(\frac{\eta^*_{max} - \eta^*_{eqc}}{\eta^*_{eqc}} \right) 100, \qquad (3)$$

where η^*_{eqc} is the efficiency for the equal commands condition, i.e., the current state-of-the-art, η^*_{max} is the maximum efficiency from map results, and $\%\Delta\eta^*$ is the efficiency gain in percentages with respect to η^*_{eqc}. The results for $\%\Delta\eta$ for all experiments are displayed in Fig. 4. A positive $\%\Delta\eta$ can be observed in all cases tested in this work. In Fig. 4 this difference is presented in terms of percentages. Results for all rotor distances are superimposed to compare how the $\%\Delta\eta$ changes with respect to rotor separation and thrust. Significant differences in behavior are evident for each rotor separation curve and in between rotors sizes. Common observations for all rotors are that the maximum value of $\%\Delta\eta$ is very similar for both mechanical and electrical efficiency. For the 11 inches rotor, maximum $\%\Delta\eta$ is 6% to 8%, for the 16.2 inches it is 4% to 6%, and for the 22 inches rotor it is about 10%. Another common feature in the results is a $\%\Delta\eta^m$ peak for throttles larger than 50%. In contrast, for $\%\Delta\eta^e$, a peak tends to show for throttle values smaller than 50%. Finally, $\%\Delta\eta^*$ tends to increase with rotor separation for all 3 rotors.

IV. CONTROL ALLOCATION STRATEGY

A. Single Coaxial Rotor

The goal of this section is to propose a control allocation strategy that tracks $\mathbf{C}_\eta$ for all operating points, considering rotor separation and which is only applicable when: i) the upper and lower rotors are equal, ii) the rotors are counter-rotating, iii) the propellers have fixed pitch, iv) the power source is the same for both rotors, and v) there is no zero net torque requirement. This excludes traditional coaxial rotor helicopters,
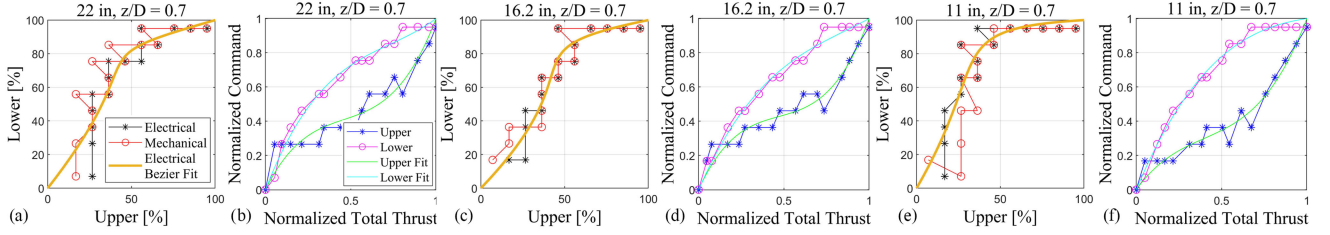
Fig. 5. Subfig. (a), (c), and (e) show individual motor commands plotted against each other for each point at $\mathbf{C}_\eta^m$ and $\mathbf{C}_\eta^e$. Note that the points for $\mathbf{C}_\eta^m$ and $\mathbf{C}_\eta^e$ fall on each other most of the time, seeming to correspond to the same operating condition. The solid yellow line is the Bezier curve fitting for the maximum efficiency control allocation implementation. Fitting was performed for the electrical efficiency points. Subfig. (b), (d), and (f) display individual motor commands plotted against normalized total thrust for each point at $\mathbf{C}_\eta^m$ and $\mathbf{C}_\eta^e$. While a), c) and e) show the Bezier fitting on the coaxial system actuation plane, in b), d), and f) the plots are mapped to its parametrization space, showing each axis of the plane as a function of the total thrust.

any other aerial vehicles with a single pair of coaxial rotors, and no other mechanism to counteract the resultant torque, such as the one in [7]. Fig. 5(a), (c) and (e) shows the result of mapping the points at $\mathbf{C}_\eta^m$ and $\mathbf{C}_\eta^e$ to their respective rotor commands. The commands from both rotors are plotted against each other. We can see that they form a curved path on the coaxial rotor actuation domain. Note also that most of the points coincide for $\mathbf{C}_\eta^m$ and $\mathbf{C}_\eta^e$. This indicates that $\mathbf{C}_\eta^m$ and $\mathbf{C}_\eta^e$ represent the same operating condition, i.e., $\mathbf{C}_\eta^m = \mathbf{C}_\eta^e$. Although Fig. 5 only illustrates a few examples, the same was observed for all experiments performed. Fig. 5 also suggests that to achieve higher efficiencies, the common strategy seems to be to keep the upper rotor command low and increase the lower rotor command to increase thrust. This is counter-intuitive, as one would expect that a higher command for the upper rotor would result in overall better efficiency, since the upper rotor is, as reported by many works [19], [20], much more efficient than the lower rotor. However, the explanation for this is that the second rotor is less efficient due to the induced flow from the upper rotor. The higher the velocity of the incoming slipstream to the lower rotor, the less efficient it is. The behavior observed in Fig. 5 seems to indicate that preventing the lower rotor from losing efficiency is a better trade-off than giving higher commands to the more efficient rotor (i.e., the upper one). A solution to extract a control allocation strategy is to find a curve that fits the points. Such curve should start from 0% of throttle and finish at 100%, for both rotors. Additionally, the curve should be parameterized so that it can correlate a linear total desired thrust command to an at least approximately linear total thrust response. These requirements are important to simplify vehicle implementation and control. We have found that Bezier curves meet all of these criteria [24]. In particular, we chose to use cubic Bezier curves, with starting and finishing points at $(0,0)$ and $(1,1)$, respectively. This range is for normalized rotor commands. With these two points fixed, two more points remain undefined to fit the shape formed by the results. The Bezier curve equation is

$$\mathbf{B}(t) = 3(1-t)^2 t \mathbf{P}_1 + 3(1-t)t^2 \mathbf{P}_2 + t^3 \qquad (4)$$

for $0 \leq t \leq 1$, where $\mathbf{B}, \mathbf{P}_1, \mathbf{P}_2 \in \mathbb{R}^2$ are points on the plane constituting the coaxial system actuation domain. To construct the Bezier curve and fit it to the shape displayed on the actuator's plane, we fit each normalized rotor command, $\mathbf{B}[y]$ for the Lower rotor and $\mathbf{B}[x]$ for the Upper, with respect to the total thrust of the system t, also normalized. Examples of this step are shown in 5 b), d) and f). With the help of the MATLAB Curve Fitting Toolbox, we fit this predefined equation to the data and

obtain the values for the points $\mathbf{P}_1$ and $\mathbf{P}_2$. These two points on the actuation domain completely define the control allocation to achieve maximal efficiency for specific rotor distance. The resulting curve fitted for electrical efficiency data is also plotted in Fig. 5. Results for all coaxial rotor sets and distances are shown in Fig. 6.

The points defining the Bezier curve are non-dimensional and can be plotted together to facilitate visualization. In Fig. 6 we also plot the points' coordinates against rotor separation. On such plots, the coordinate with the largest variation across rotor separation is $\mathbf{P}_1[x]$, which decreases in value with increased rotor distance. This parameter variation reflects the tendency for the maximum efficiency commands to converge to the line of equal commands with decreasing rotor separation. This confirms the Fig. 4 results and is more evident for the rotors with propellers with diameters of 22 and 11 inches. Once again, the 16.2 inches set demonstrates less variation with respect to rotor separation. Another observation is that the x coordinate of point $\mathbf{P}_1$ increases in value with increased rotor size, shifting this point to the right when comparing Fig. 6(a), (c) and (e).

B. Coaxial Multirotor Vehicle

Here, we describe how to implement the method on an octocopter, as presented in Fig. 1 c). The control allocation for a regular multirotor vehicle is

$$\mathbf{T}_i = \mathbf{\Gamma}^\dagger \begin{bmatrix} \tau_x & \tau_y & \tau_z & T \end{bmatrix}^T, \qquad (5)$$

The right-hand side of the equation include the control outputs to stabilize the vehicle, where τ_* is the desired torques output in each direction from the vehicle attitude controller, and T is the total desired thrust. On the left-hand side $\mathbf{\Gamma}^\dagger$ is the pseudo-inverse of the constant control allocation matrix, $\mathbf{\Gamma}$ [25], and $\mathbf{T}_i$ is the vector of desired thrusts for each individual rotor. In (5), each column of $\mathbf{\Gamma}^\dagger$, here denoted by $\gamma_x^\dagger$, $\gamma_y^\dagger$, $\gamma_z^\dagger$, and $\gamma_T^\dagger$, accounts for the contribution each controller command has to the total thrust of each individual rotor. To implement the proposed control allocation, we split the solution into

$$\mathbf{T}_i = \mathcal{B}\left(\begin{bmatrix} \gamma_x^\dagger & \gamma_y^\dagger & 0 & \gamma_T^\dagger \end{bmatrix} \begin{bmatrix} \tau_x & \tau_y & \tau_z & T \end{bmatrix}^T \right)$$
$$+ \begin{bmatrix} 0 & 0 & \gamma_z^\dagger & 0 \end{bmatrix} \begin{bmatrix} \tau_x & \tau_y & \tau_z & T \end{bmatrix}^T \qquad (6)$$

and apply the map $\mathcal{B}$ to the first term of the right-hand side. This map transforms the total desired thrust for each coaxial rotor pair to individual rotor commands, as in (4). Note that here
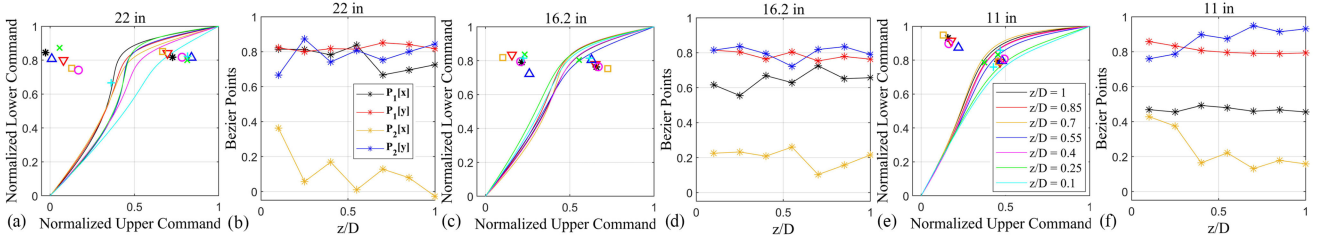
Fig. 6. The plots in (a), (c), and (e) are the Bezier curve fittings for the rotor commands obtained from the points at the maximum efficiency boundary for electrical efficiency. For each rotor set, the curves for all rotor separations are superimposed. The points defining each Bezier curve are shown as color-matching markers. The plots in (b), (d), and (f) show how the x and y coordinates of the Bezier curve points change with respect to rotor separation.
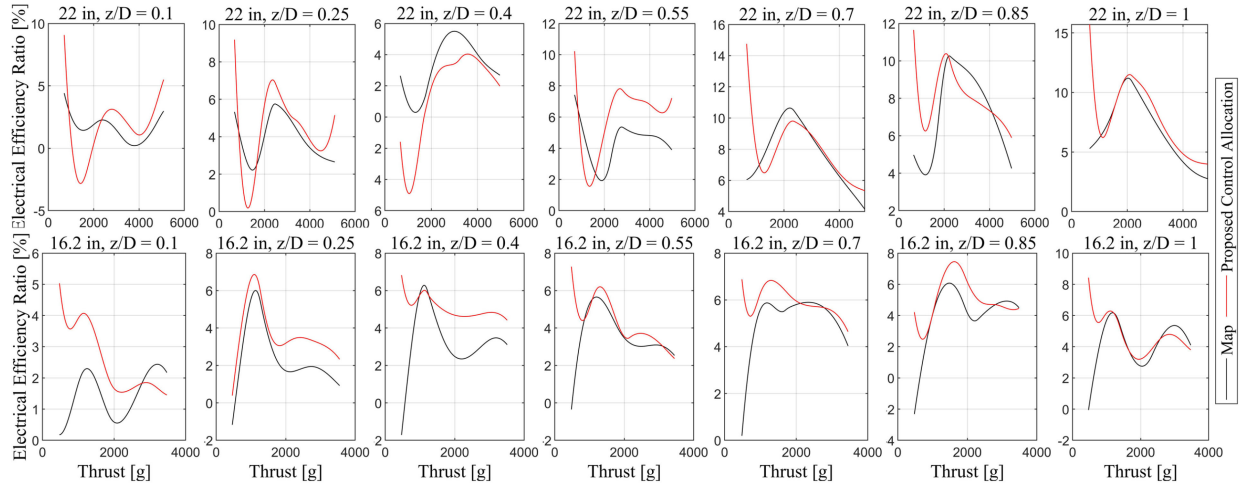

Fig. 7. Results for the control allocation validation experiments. The black lines show $\%\Delta\eta$ results are from the mapping experiments. The red lines represent $\%\Delta\eta$ for the proposed control allocation method. Results for the 22 inches pair are shown in the first row of plots (a), (b), (c), (d), (e), (f), and (g), while results for the 16.2 inches pair are shown in the second row with sub-figures (h), (i), (k), (l), (m), (n), and (o).

$\mathbf{T}_i$ is treated as being analogous to rotor commands. In reality, the relationship between the two is complex and non-linear, but monotonically related. Nonetheless, such approach allows to satisfy τ_x, τ_y and T while tracking $\mathbf{C}_\eta$. By leaving the yaw control out of the effect of this map, it is still possible to satisfy τ_z with differential velocity control of individual rotors, as in the current standard. It is possible that correcting for yaw introduces disturbances in the control allocation tracking $\mathbf{C}_\eta$, making it operate slightly off of $\mathbf{C}_\eta$. However, such corrections are often brief and they don't affect flight endurance.

V. CONTROL ALLOCATION IMPLEMENTATION RESULTS

A. Static Experiments

To validate the proposed control allocation method, we performed static tests on the platform and compared them with the mapping experiments. To avoid inconsistencies originating from changes in temperature, humidity, or positioning differences between experiments, all mapping tests were rerun and directly followed by the control allocation validation, obtaining reliable results. The fitted control allocation was discretized into 13 points equally spaced with respect to the parameter t in (4), and tests followed the procedure described in Section III-A. Even though mapping experiments were performed again for

all rotor sets, control allocation tests were done only for the rotors with propellers of diameters of 16.2, 22, and 11 inches for $z/D = 0.7$. Fig. 7 shows the results for $\%\Delta\eta^e$ of such experiments, following the format and procedure used for Fig. 4. In all cases, $\%\Delta\eta^e$ results from the proposed control allocation method followed the same behavior as the results from the mapping experiments (Fig. 4). For the 16.2 inches rotor, the new control allocation displayed slightly larger $\%\Delta\eta^e$ for the better part of the thrust range for all rotor separations. For the 22 inches rotor, results are more diverse, with regions of larger and smaller $\%\Delta\eta^e$.

The most likely reason for such differences is that the Bezier curves yielded different commands from those obtained on the mapping, following the best fit. This is expected since the mapping resolution was relatively coarse (only 10×10 points). At the same time, the Bezier fitting produces a continuous curve which most of the time crosses between the zig-zagging of the command points (see Fig. 5). Lastly, Fig. 8 shows the variation of total coaxial thrust and torque with respect to throttle command as parameterized on the proposed control allocation. As expected, the net torque resulting from the control allocation is not zero. Since the strategy is to keep the upper rotor at low throttle and increase the lower rotor throttle to increase thrust, significant portions of the torque generated by the lower rotor are not countered by the counter-rotating upper rotor. In
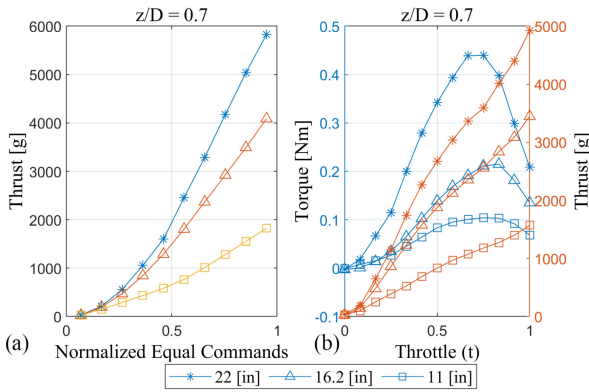
Fig. 8. Sub-figure (a) shows the thrust response from the coaxial systems to equal commands for reference. Despite high nonlinearity, that is the current standard throttle control allocation for coaxial multirotor vehicles. Sub-figure (b) shows torque and thrust results from the control allocation validation experiments. The measurements are plotted against the parameterized throttle command proposed in the control allocation. As expected, the resultant torque is not zero, and the thrust response is monotonic and approximately linear.
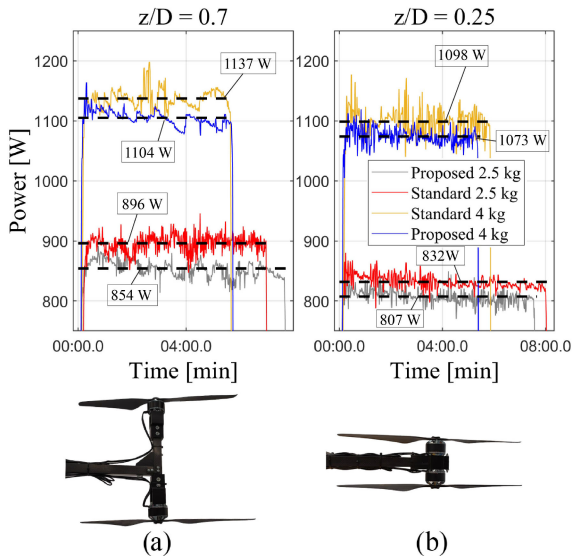

Fig. 9. Flight test results show power measurements taken onboard the vehicle. It includes two payload scenarios comparing the performance of the state-of-the-art and the proposed control allocation. The proposed method provides an 8.7 % flight time increase for the larger payload and 1.9 % for the smaller payload.

the implementation case, such resultant torque is compensated by another coaxial rotor unit with all rotors rotating in the opposite direction, as it is the standard for flat multirotors, i.e., non-coaxial rotor vehicles.

B. Vehicle Experiments

The octocopter platform illustrated in Fig. 1 was designed with two variations. The one in the picture has propellers that are separated with $z/D = 0.7$, which is the distance that provides the highest efficiencies for mid-range throttle. The other version has the motor attached as close as possible to each other considering the mounting structure, resulting in $z/D = 0.25$, as in Fig. 9 b) and commonly found in the literature and industry [4], [5], [8]–[10]. Both versions use 400 KV motors with 16 inches and

TABLE II
OCTOCOPTER TEST RESULTS

z/D	Payload [kg]	$\eta^e New$ [g/W]	$\eta^e Standard$ [g/W]	%$\Delta\eta^e$
0.7	2.5	7.436	7.087	4.924 %
	4	7.11	6.904	2.983 %
0.25	2.5	7.435	7.211	3.106 %
	4	6.99	6.831	2.327 %

run a PX4 firmware on a Pixhawk 4 flight controller. Together with a 6 cells Li-Po battery of 6000 mAh used for testing, the $z/D = 0.7$ version weighs 3.85 kg, while the $z/D = 0.25$ version weighs 3.5 kg. To verify the feasibility of the proposed control allocation, we performed manual hovering flight tests with the standard PX4 firmware and a modified version of the firmware to accommodate the proposed method. To test the different operating points, weights of 2.5 kg, and 4 kg were attached to the system, simulating payloads, and 8 tests were performed.

Starting with a fully charge battery, in the experiments the pilot controlled the vehicle to hover in the same spot around 0.5 m off of the ground, and only land when the battery reached around 40% to 30% of its capacity. Here, we are mostly interested in the power and efficiency at hover. Flight time results were not as consistent due to the batteries used being at different stages of use, where some had reduced charge holding capacity, despite having the same label rating and weight of 845 g. Despite the propeller models not being the same as in the static tests, for the modified controller experiment the parameters used to define the Bezier curve were extracted from the results of the 16.2 inches rotor. When testing the $z/D = 0.7$ version, the values are $\mathbf{P}_1(x) = 0.77$, $\mathbf{P}_1(y) = 0.75$, $\mathbf{P}_2(x) = 0.1$, and $\mathbf{P}_2(y) = 0.81$. For the $z/D = 0.25$ version, the values are $\mathbf{P}_1(x) = 0.55$, $\mathbf{P}_1(y) = 0.8$, $\mathbf{P}_2(x) = 0.23$, and $\mathbf{P}_2(y) = 0.84$.

The data was collected using the onboard sensors in the Pixhawk 4 and its PM7 power board. These include battery voltage and total current consumed. Results are presented in Fig. 9. The graphs in Fig. 9 show the vehicle power consumption to hover and battery levels across flight time, comparing both the current state-of-the-art and the proposed control allocation, divided in two, for $z/D = 0.7$ and $z/D = 0.25$. The proposed control allocation required less power consumption for all tests. Table II summarises the key results from such experiments. It is interesting to note that despite using different propellers in the vehicle from the static tests, the octocopter experiments corroborate with the static test result trends. This indicates that the proposed control allocation is robust, allowing for implementation uncertainties. Results show that farther apart rotors have a larger %$\Delta\eta$ compared to coaxial rotors with smaller z/D. Second, the power consumption using the proposed method for $z/D = 0.7$ reaches similar levels to standard control allocation for $z/D = 0.25$, despite the latter being 350 g lighter. It is likely that a weight-optimized design for large z/D could be more efficient with the proposed method than a vehicle with small z/D, especially for larger payloads. Besides the change in control allocation, no other modifications were made on the vehicles between the tests for the proposed and regular control allocations, which were performed one after the other, giving time for the motors to cool down. There was no noticeable difference between the two control methods for the pilot performing the tests, and no tuning was required when switching between them.

All tests ran with the default PX4 controller gains. However, for reasons unknown to the authors, the vehicle with $z/D = 0.25$ was harder to control than the one with $z/D = 0.7$, especially for the heavier payload case, as indicated by the noisier data.

VI. Conclusion

This work presented an open-source benchmarking platform for coaxial rotor systems that allows us to analyse and improve their efficiency and a map of the whole actuation domain of coaxial systems that relies on extensive experiments performed with the platform. Findings include:

- The map of efficiency against thrust obtained for the whole actuation domain of the coaxial rotor exhibits a clear upper boundary, and every thrust setpoint along the range has an operating point on this boundary.
- For most of the thrust range, sending equal commands to both rotors results in sub-optimal efficiencies.
- For all rotors tested, the maximum value for $\%\Delta\eta$ is very similar for mechanical and electrical efficiencies.
- For all rotors tested, the efficiency gain, $\%\Delta\eta$, tends to increase with rotor separation.
- Maximum efficiency commands tend to converge to the equal commands line with decreasing rotor separation.
- Mechanical and electrical maximum efficiency boundaries typically represent the same operating conditions.

Furthermore, we proposed a control allocation method that successfully reproduces the maximum efficiency boundary, improving efficiency up to 11% over the industry standard. Additionally, implementation on an octocopter with 4 sets of coaxial rotors, 2 different payload scenarios, and 2 rotor spacings showed that switching to the new, more efficient control allocation is seamless, with no re-tuning required.

References

[1] S. Bouabdallah, P. Murrieri, and R. Siegwart, "Design and control of an indoor micro quadrotor," in *Proc. IEEE Int. Conf. Robot. Automat.*, 2004, vol. 5, pp. 4393–4398.

[2] P. Pounds, R. Mahony, P. Hynes, and J. M. Roberts, "Design of a four-rotor aerial robot," in *Proc. Australian Conf. Robot. Automat.*, 2002, pp. 145–150.

[3] "Open source autopilot for drones- PX4 Autopilot," Jul. 2022. Accessed: Aug. 15, 2021. [Online]. Available: https://px4.io/

[4] K. Bodie et al., "Active interaction force control for contact-based inspection with a fully actuated aerial vehicle," *IEEE Trans. Robot.*, vol. 37, no. 3, pp. 709–722, Jun. 2021.

[5] W. Ong, S. Srigrarom, and H. Hesse, "Design methodology for heavy-lift unmanned aerial vehicles with coaxial rotors," in *Proc. Amer. Inst. Aeronaut. Astronaut. Scitech Forum*, 2019, Art. no. 2095.

[6] S. D. Prior, "Reviewing and investigating the use of co-axial rotor systems in small UAVs," *Int. J. Micro Air Veh.*, vol. 2, no. 1, pp. 1–16, 2010.

[7] J. Buzzatto, P. H. Mendes, N. Perera, K. Stol, and M. Liarokapis, "The new dexterity omnirotor platform: Design, modeling, and control of a modular, versatile, all-terrain vehicle," in *Proc. IEEE/RSJ Int. Conf. Intell. Robots Syst.*, 2021, pp. 6336–6343.

[8] EHang, "Electric passenger-grade autonomous aerial vehicle," Jul. 2021. Accessed: Aug. 12, 2021. [Online]. Available: https://www.ehang.com/ehangaav

[9] Airspeeder, "The world's first racing series for electric flying cars," Jul. 2021. Accessed: Aug. 12, 2021. [Online]. Available: https://airspeeder.com/

[10] D. D. C. League, "Big drone," Jul. 2021. Accessed: Aug. 12, 2021. [Online]. Available: https://dcl.aero/explore/big-drone/

[11] R. D. Lorenz et al., "Dragonfly: A rotorcraft lander concept for scientific exploration at titan," *Johns Hopkins APL Tech. Dig.*, vol. 34, no. 3, pp. 374–387, 2018.

[12] M. Brazinskas, S. D. Prior, and J. P. Scanlan, "An empirical study of overlapping rotor interference for a small unmanned aircraft propulsion system," *Aerospace*, vol. 3, no. 4, 2016, Art. no. 32.

[13] Y. Lei, Y. Bai, Z. Xu, Q. Gao, and C. Zhao, "An experimental investigation on aerodynamic performance of a coaxial rotor system with different rotor spacing and wind speed," *Exp. Thermal Fluid Sci.*, vol. 44, pp. 779–785, 2013.

[14] B. Theys, G. Dimitriadis, P. Hendrick, and J. De Schutter, "Influence of propeller configuration on propulsion system efficiency of multi-rotor unmanned aerial vehicles," in *Proc. IEEE Int. Conf. Unmanned Aircr. Syst.*, 2016, pp. 195–201.

[15] J. E. Holzsager, *The Effects of Coaxial Propellers for the Propulsion of Multirotor Systems*, M.Sc. thesis, Dept. Mech. Aerosp. Eng. New Brunswick, NJ, USA: The State Univ. New Jersey, 2017.

[16] K.-S. Min, B.-J. Chang, and H.-W. Seo, "Study on the contra-rotating propeller system design and full-scale performance prediction method," *Int. J. Nav. Archit. Ocean Eng.*, vol. 1, no. 1, pp. 29–38, 2009.

[17] J. Chebbi, F. Defaÿ, Y. Brière, and A. Deruaz-Pepin, "Novel model-based control mixing strategy for a coaxial push-pull multirotor," *IEEE Robot. Automat. Lett.*, vol. 5, no. 2, pp. 485–491, Apr. 2020.

[18] R. S. McKay, M. J. Kingan, S. T. Go, and R. Jung, "Experimental and analytical investigation of contra-rotating multi-rotor UAV propeller noise," *Appl. Acoust.*, vol. 177, 2021, Art. no. 107850.

[19] M. Ramasamy, "Hover performance measurements toward understanding aerodynamic interference in coaxial, tandem, and tilt rotors," *J. Amer. Helicopter Soc.*, vol. 60, no. 3, pp. 1–17, 2015.

[20] G. J. Leishman, *Principles of Helicopter Aerodynamics With CD Extra*. New York, NY, USA: Cambridge Univ. Press, 2006.

[21] J. G. Leishman and M. Syal, "Figure of merit definition for coaxial rotors," *J. Amer. Helicopter Soc.*, vol. 53, no. 3, pp. 290–300, 2008.

[22] C. P. Coleman et al., *A Survey of Theoretical and Experimental Coaxial Rotor Aerodynamic Research*, CA, USA: NASA Ames Research Center, Moffett Field, Tech. Paper NASA-TP-3675, Mar. 1997.

[23] J. D'Errico, "SLM - shape language modeling," Jul. 2021. Accessed: Jun. 20, 2021. [Online]. Available: https://www.mathworks.com/matlabcentral/fileexchange/24443-slm-shape-language-modeling

[24] H. Prautzsch, W. Boehm, and M. Paluszny, *Bézier and B-Spline Techniques*, vol. 6. Berlin, Germany: Springer, 2002.

[25] R. Mahony, V. Kumar, and P. Corke, "Multirotor aerial vehicles: Modeling, estimation, and control of quadrotor," *IEEE Robot. Automat. Mag.*, vol. 19, no. 3, pp. 20–32, Sep. 2012.